metals

MDPI

Article

Mechanical Properties of LPBF-Built Titanium Lattice Structures—A Comparative Study of As-Built and Hot Isostatic Pressed Structures for Medical Implants

Benedikt Adelmann * and Ralf Hellmann

Applied Laser and Photonics Group, Faculty of Engineering, University of Applied Sciences Aschaffenburg, Wuerzburger Strasse 45, 63734 Aschaffenburg, Germany
* Correspondence: benedikt.adelmann@th-ab.de

Abstract: We compare different lattice structures with various elementary cell sizes built by laser powder bed fusion with and without hot isostatic pressing as post treatment. Cylindrical lattice structures are mechanically tested upon static and dynamic load in order to achieve high elasticity, high fracture strength and a high number of cycles to failure with respect to applications as medical implants. Evaluating the Young's modulus, a high stiffness for the body diagonal structure and a low fracture stress for the G-structure are measured. Hot isostatic pressing results in a higher Young's modulus and is ambiguous in terms of fractural stress. While samples without hot isostatic pressing reveal a shear fracture, the hot isostatic pressed samples have a high ductile area where the lattice layers are wrapped and pressed into the underlying layers without a fracture. Under dynamic load, the samples without hot isostatic pressing mostly are unable withstand 10^6 cycles at typical loads of the human body. Hot isostatic pressing has no significant influence on the strength at high loads and low cycle numbers, but at low loads all samples survived 10^6 cycles. As a consequence, dode-thick and rhombic dodecahedrons with 2 mm and 1.5 mm lattice size after hot isostatic pressing are recommended for medical implants because of the high elasticity, high fracture stress and high resistance against dynamic loads, which fulfill implant requirements.

Keywords: additive manufacturing; laser powder bed fusion; titanium; lattice structures; medical implant

Citation: Adelmann, B.; Hellmann, R. Mechanical Properties of LPBF-Built Titanium Lattice Structures—A Comparative Study of As-Built and Hot Isostatic Pressed Structures for Medical Implants. *Metals* **2022**, *12*, 2072. https://doi.org/10.3390/met12122072

Academic Editors: Changjiang Pan, Jingan Li and Pavel Krakhmalev

Received: 28 September 2022
Accepted: 23 November 2022
Published: 2 December 2022

1. Introduction

Life expectancy rises continuously worldwide, changing the age structure of the population pyramid. This socio-demographic change impacts social and commercial prospects and creates increasing and new demands for care and medical technologies. Next to the therapy of degenerative diseases of the central nervous system, preserving mobility is a key requirement that inevitably challenges the medical technology sector [1–3].

Laser powder bead fusion (LPBF), also denoted as selective laser melting [4], features the potential for improving medical implant design, in turn improving the mobility of invalid and older people. Specifically, medical grade titanium alloys are in favor for implants because of their superior biocompatibility [5–12]. Today, spinal implants are primarily manufactured by casting or milling. Though implant technology is quite advanced, milled implants still exhibit deficits, such as stress shielding, due to the high stiffness of implants as compared to natural tissue. Stress shielding results in a capacity underload of the protected natural bone, leading in a reduction in bone density and weakening of healthy bone tissue. Stress shielding appears when the inserted implant mechanically buffers the remaining tissue, destabilizing the balance of formation and degradation in bone tissue [13]. In order to circumvent stress shielding in LPBF-made implants, Fousová et al. built complex lattice structures of 316L stainless steel to copycat the mechanical elasticity of the trabecular human bone [14]. By producing porous materials using LPBF, stress shielding was reduced by 75% as compared to solid implants [15]. Printing porous implants of β-Ti-35Zr-28Nb

using LPBF has led to a porosity of up to 83% and a Young's modulus in the range of trabecular bone [5]. In particular, LPBF allowed variance of Young's modulus by one order of magnitude, thus avoiding stress shielding [16]. Porous structures built from Ti16Nb by powder metallurgy using different amount of powders have shown mechanical properties similar to human bones [17]. LPBF even allows a mixture of powders like hydroxyapatite (a matrix for bones) and 316L stainless steel to produce a material with tensile strengths close to human bones [18]. Altogether, these results underline that different lattice structures can improve the elasticity and avoid possible stress shielding.

Beside such considerations as the Young's modulus and stress shielding, a medical implant has to last for several decades under dynamic loads, i.e., a high number of stress cycles. Therefore, the fatigue behavior of the implant is also of utmost importance and has thus been widely studied [6,19–21]. With respect to LPBF, the fatigue behavior is strongly negatively influenced by pores slightly underneath the surface [22] and from particles on the surface [23,24]. Because the position of such defects has a major influence, the fatigue behavior is hard to predict by fracture models [25,26].

With increasing defect size, the fatigue resistance decreases [27], so the LPBF process parameters have to be carefully adjusted. The microstructure during the solidification of the LPBF process also influences the fatigue behavior [28]. As LPBF parts do not adequately meet the requirements for implants, e.g., high service life and defect-free microstructure [29], post-treatment is compulsory according to ASTM F2924–14. In this respect, hot isostatic pressing (HIP) is well recognized for a reduction of inner pores and cavities as well as for an increase in density [30,31]. Studies have revealed that HIP treatment of Ti–6Al–2Zr–1Mo–1V results in a 15% increase in tensile strength and a 53% increase in ductility [32]. Moreover, hot isostatic pressing significantly reduces the residual stress in LPBF built parts. This typically results in an increase of fracture toughness and thus in a significantly stronger plastic area, as reported for aluminum alloys [33], stainless steel [34] and special alloys [35]. This in turn leads in titanium to an improved number of cycles to failure due to hot isostatic pressing [36,37]. In addition, unwanted anisotropy like build direction–dependent strength can be removed [38,39]. For Ti–6Al–2Zr–1Mo–1V, the tensile strength and ductility of the HIP specimens at 500 °C have been reported as 14.8% and 52.8% higher than those of their counterparts [32], respectively.

In addition to the often-used Ti-6Al-4V, other titanium-based alloys are under study to improve the mechanical properties of implants. For instance, Mo2C/Ti64 composites reveal a remarkable improvement of 23% higher hardness and 20% higher tensile strength by adding Mo2C [40]. Ti–16Nb–xZr alloys have been studied [41], showing advantages in terms of cost and easy manufacturability as compared to other titanium alloys. Compared to titanium, Ti-Nb alloys are characterized by a higher hardness and transverse rupture strength, while simultaneously the elastic modulus is decreased [42].

The underlying metallographic properties and processes during LPBF and hot isostatic pressing of medically relevant titanium alloys have been comprehensively studied in previous works. To guide the reader to further reading, we refer to [31,32,43], while in this contribution we focus on a comparative study of different lattice structures.

Because the fatigue behavior of LPBF built structures depends strongly on the build geometry [44], e.g., thin wall-based structures have a better fatigue resistance than lattice structures [45,46], each structure in combination with a thermal post process has to be tested individually towards fatigue behavior. Therefore, in this contribution, lattice structures for medical implants, adopted by the commonly utilized Materialise Magics® software (Ver. 25.3, Leuven, Belgium), are examined, and the influence of hot isostatic post processing on the strength, elasticity and fatigue behavior of these lattice structures is evaluated and discussed in terms of fulfillment of the requirements of the medical application.

With respect to geometrical restrictions, the size of typical intervertebral disc implants varies in the range of 5 mm to 11 mm in height, from 6 mm to 19 mm in width and from 12 mm to 18 mm in depth [47]. Footprints of implants vary from circles and triangles to rectangles, ovals, kidney shapes and curved geometries [47]. For the typical load, different

typical postures have to be considered. Typical forces on the intervertebral disc are 0.7 kN when sitting, 1.9 kN when lifting 10 kg and 9 kN when lifting 50 kg [48]. Therefore, a movement that is performed once a day results after 30 years in about 10^4 movements. Assuming that a weight of 50 kg should not be lifted several times a day, for the load of 9 kN about 10^4 cycles is enough. At the same time, weights of 10 kg are lifted very often tens of times a day depending on the motion activity of a person, so an implant has to last 10^6 cycles. In everyday life, the typical internal pressure in an intervertebral disc is 2 MPa, and a symmetrically loaded intervertebral disc collapses at a load of 11 MPa. Therefore, we also want to prove whether LPBF built lattice structures fulfill these requirements.

2. Experiment

2.1. Materials

The material used for the experiments is Ti-6Al-4V Grade 23 (Heraeus, Hanau, Germany) with the material number 3.7165, which is one of the most often used titanium alloys for medical applications. According to the datasheet, the density of 4.43 g/cm^3 classifies the material as lightweight alloy. The material is characterized by a high strength at low density, an excellent corrosion resistance and high biocompatibility. Due to a low amount of interstitial iron and oxygen (below 0.3 wt%), the material is suitable for medical implants and dentistry implants. In detail, the alloy consists of 6 wt% aluminum and 4 wt% vanadium, which is balanced with titanium. The material is powder, with a grain size between 15 µm and 53 µm and the particles having a spherical shape. According to the datasheet, the tensile strength is 1280 MPa as built and 960 MPa after heat treatment. Further, the Young's modulus is given with 115 GPa as built and 125 GPa after heat treatment.

Regarding the high cooling rate during LPBF, Ti-6Al-4V represents an α-martensite after the additive manufacturing process. Upon hot isostatic pressing below the β-transus temperature of 980 °C, the crystalline structure of the metal is transformed to a mixture of α and β fractions, which are often lamellar shaped. The material then still includes proportions of pure α-martensite phases. For temperatures above the β-transus point during HIP treatment, large β-grains develop, which alter to a lamellar-shaped α–β mixture when cooling down after the heat treatment [43,49] and influence the mechanical properties towards higher cutting forces during milling and higher ductility [9,49].

2.2. Lattice Structures

To achieve the targeted high elasticity, 5 different lattice structures, chosen and adopted utilizing Materialise Magics® software, as shown in Figure 1, are studied. The body diagonal structure has a cubic elementary cell with round bars and rounded nodes on the intersection points. The diamond 30% density structure (hereafter named diamond) also consists of round bars, building a diamond elementary cell, but has no rounding on the intersection points. In addition, with round bars and no rounding on the intersection point, a rhombic dodecahedron elementary cell is built. The dode-thick structure is built from triangular bars without rounding at the intersection point. The G-structure has the same elementary cell as the body diagonals but uses triangular bars with no rounding at the intersection points. All structures are constructed using the "Materialize Magic Structures" toolbox.

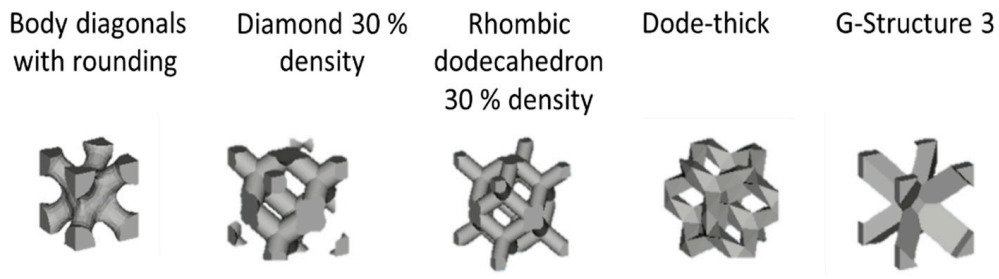

Figure 1. Scheme of different lattice structures.

2.3. LPBF Process

We employed a Lasertec 30 machine (DMG Mori Additive, Bielefeld, Germany) for the LPBF of Ti-6Al-4V (material number 3.7165), building cylinders with dimensions of 10 mm and 15 mm in diameter and height, in accordance with DIN 50106 "Testing of metallic materials—Compression test at room temperature". This size is in the range of typical intervertebral disc implants. The volume was filled by five different lattice structures using the software Materialize Magics, as shown in Figure 1. In total, three variations of the test specimen were created per unit cell. The size of the elementary cell was varied between 1 mm, 1.5 mm and 2 mm. The layer height during the LPBF process was 50 µm. The employed laser machine parameters were a scan velocity of 0.74 m/s, a laser power of 220 W and hatch distance of 0.10 mm. The scan strategy was to fill the necessary areas with lines, whose angle changes from layer to layer. After this infill, the borderlines of the edges were scanned by the laser beam. For the built parts, this parameter combination led to a comparatively low surface roughness R_a of about 10 µm and a high density.

2.4. Hot Isostatic Pressing

The machine used for hot isostatic pressing was a Q15L 2070-1400M from Quintus Technologies AB (Vasteras, Sweden). The system provides a maximum pressure of 200 MPa and a maximal temperature of 1400 °C under argon atmosphere. The process chamber is 300 mm in height and 170 mm in diameter, which allows a maximum load of 40 kg. The temperature control has an accuracy of ±10 °C and provides a maximum heating rate of 30 °C/min.

Hot isostatic pressing cycles were performed in accordance with ASTM F2924–14, which translates to treatment with 100 MPa pressure at a temperature of 925 °C for a 3 h period. In detail, the HIP process was divided into four steps. In the first step, the process chamber is heated to 890 °C, with a heating rate of 10°/min and simultaneously the pressure is increased to 100 MPa. During the second step, the heating rate is reduced to 3°/min up to a temperature of 925 °C, to avoid overshooting. In a third step, the temperature (925 °C) and pressure (100 MPa) are held for 3 h before the chamber cools down slowly due to natural heat conduction in the fourth step, which takes several hours.

To avoid confusion, in this contribution, samples undergoing HIP are named as post HIP, while samples measured before the HIP process are referred to as pre-HIP.

2.5. Mechanical Testing

Compressive strength measurements were performed with a universal testing machine Shimadzu Autograph AG-X plus (Shimadzu, Kyoto, Japan), using a speed of 1 mm/min. The compressive fatigue behavior tests were carried out on the dynamic tensile test rig STEPLab UD020 (STEPLab, Resana, Italy). A sinusoidal stress–time function with a frequency of 10 Hz and with a force between 0 N and the nominal value was used. The specimens were run through the loading case until either a break occurred or 10^6 cycles were reached. A total of three measurements were made for each load case. The resulting cycles to failure were recorded in a Wöhler curve (S–N curve). For all mechanical tests, three samples per group were used in order to achieve a reliable value and its deviation.

3. Results

3.1. Print Characteristics

To characterize printing, the relative density of the lattice structures was determined, and cross-section images were taken. To determine the relative density, the surrounding volume of the cylinders was measured, and the samples were weighed. The weight was divided by the volume and the density of solid Ti-6Al-4V. The results are shown in Figure 2 for the five lattice structures with the three elementary cell sizes under study. The results reveal decreasing densities with increasing elementary cell sizes for all cell types except the G-structure. A possible reason for this is that the size of the rods is smaller to the minimum producible size of the laser machine. As a consequence, the rods are produced larger than

designed, and the density increases. For larger elementary cell size, these rods are designed larger, and the oversizing of the machine is reduced. A comparison between the cell types reveals the highest density for body diagonals and the rhombic dodecahedron and the lowest for the G-structure.

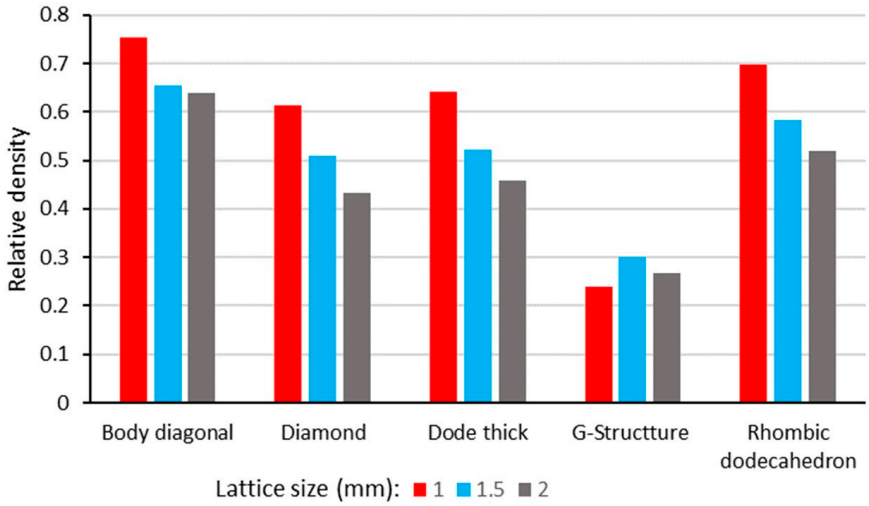

Figure 2. Relative density of different lattice structures.

To study porosity, cross-section images were taken from both pre- and post-HIP specimens (cf. Figure 3. As depicted in Figure 3a, the porosity is quite low, but there are pores with sizes up to about 50 µm. Several further cross-section images reveal that pores are distributed in many areas all over the sample. After the HIP process (Figure 3b), no pores were visible. When analyzing several cross-section images, it was observed that after HIP, the size and number of pores were reduced as compared to pre-HIP.

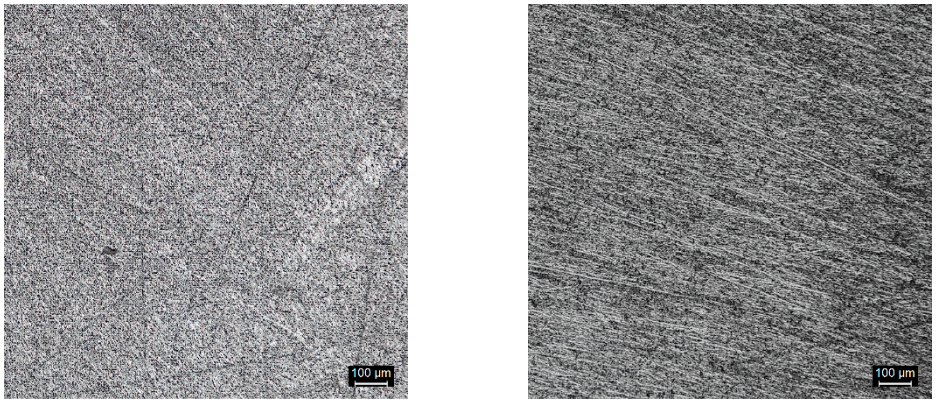

(**a**) (**b**)

Figure 3. Cross-section images (**a**) without HIP and (**b**) after HIP.

3.2. Stress–Strain Behavior

To exemplify the stress–strain properties of the evaluated lattice structures, Figure 4 summarizes the stress–strain behavior of the dode-thick structure for different lattice sizes before and after hot isostatic pressing. It should be noted that the stress–strain behavior of the other lattice structures under investigation reveals similar qualitative characteristics and quantitative results such as the Young's modulus and fracture stress, the results of which will be shown in Section 3.3 (Figures 6 and 7).

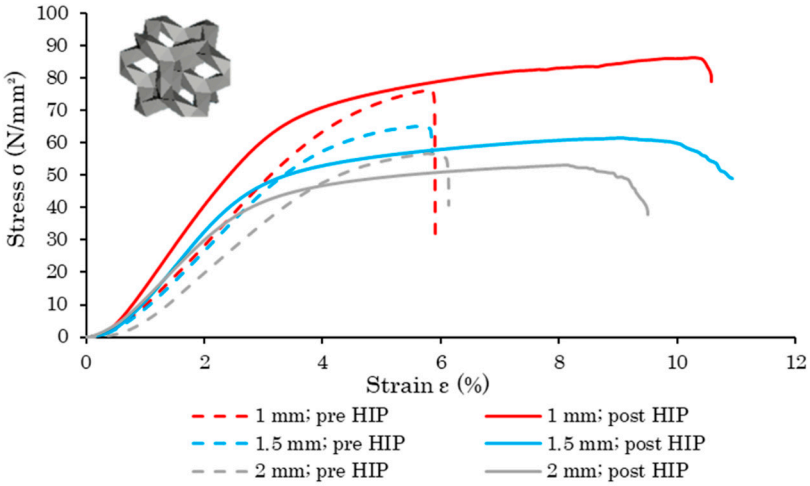

Figure 4. Stress–strain diagram of a dode-thick lattice structure.

As the results in Figure 4 show, after hot isostatic pressing, the elasticity reveals, in accordance with Ref. [49], a higher stiffness as compared to the pre-HIP state for all structure sizes. With decreasing elementary cell size, both stiffness and fracture strength increase for both pre-HIP and post-HIP structures, a trend that was previously shown for body-centered cubic Ti-6Al-4V lattices (without hot isostatic pressing) by Maskery et al. [50]. In addition, the diagram reveals a significantly higher strain of the post-HIP samples, caused by an extended range of plastic deformation. This agrees with the literature results, revealing a substantial ductility improvement for SLM-built titanium samples [31], which in turn is associated with the characteristic fracture and compression behavior of the pre-HIP and post-HIP structures. Figure 5 depicts the samples after the compression test, showing that the pre-HIP samples in Figure 5a are characterized by a shear fracture through the complete sample, as is typical for brittle structures. Contrary to this, the post-HIP samples in Figure 5b do not show any fracture rather than a strong deformation of the entire lattice structure, with layers being pressed into the underlying layers. This can be attributed to a fracture strain increase of up to 14% after thermal post treatment, while at the same time the yield stress decreases, as was reported for Ti-6Al-4V by Vrancken et al. [43]. Similar experiments for nickel-based superalloys show a 410% higher ductility after a HIP treatment, followed by a solid solution heat treatment [51].

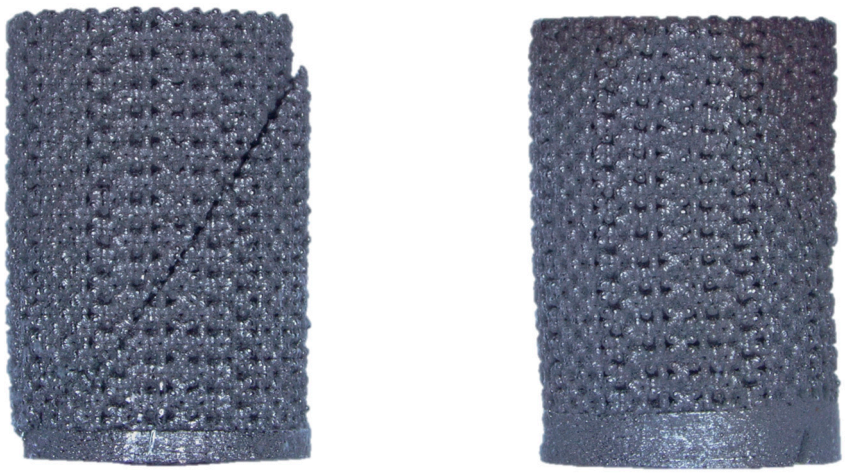

(**a**) (**b**)

Figure 5. Failure of dode-thick lattice structures with 10 mm diameter under static load before HIP (**a**) and after HIP process (**b**).

3.3. Elasticity and Strength

To identify the most suitable lattice structure and elementary cell size in terms of high elasticity and to avoid stress shielding and damage under a single high load, as for lifting a very heavy object, the Young's modulus and the fractures stress under static load were determined. Figure 6 gives an overview of the Young's modulus for the different lattice structures and elementary cell sizes under study, as well as for specimens without and with hot isostatic pressing. For all specimens, hot isostatic pressing leads to an increasing stiffness in the range between 10% and 20%. Furthermore, for all lattice structures except the G-structure, Young's modulus increases with decreasing elementary cell size. A disadvantage of small elementary cell sizes is a higher standard deviation, which can be attributed to the smaller web thickness, for which SLM's typical defects, such as pores, have a higher influence. In addition, comparing the lattice structures amongst each other, the G-structure exhibits the lowest, whereas the Body diagonal structure exhibits the highest Young's modulus. Diamond and dode-thick structures reveal similar elasticity, while rhombic dodecahedrons appear slightly stiffer. In this context, the Young's modulus is dependent on the relative density (see Figure 2), while the Body diagonal has the highest relative density and the highest Young's modulus and the G-structure is lowest in both categories. For diamond and dode-thick structures, the Young's modulus and the relative density are similar, and the rhombic dodecahedron is slightly higher in both density and Young's modulus.

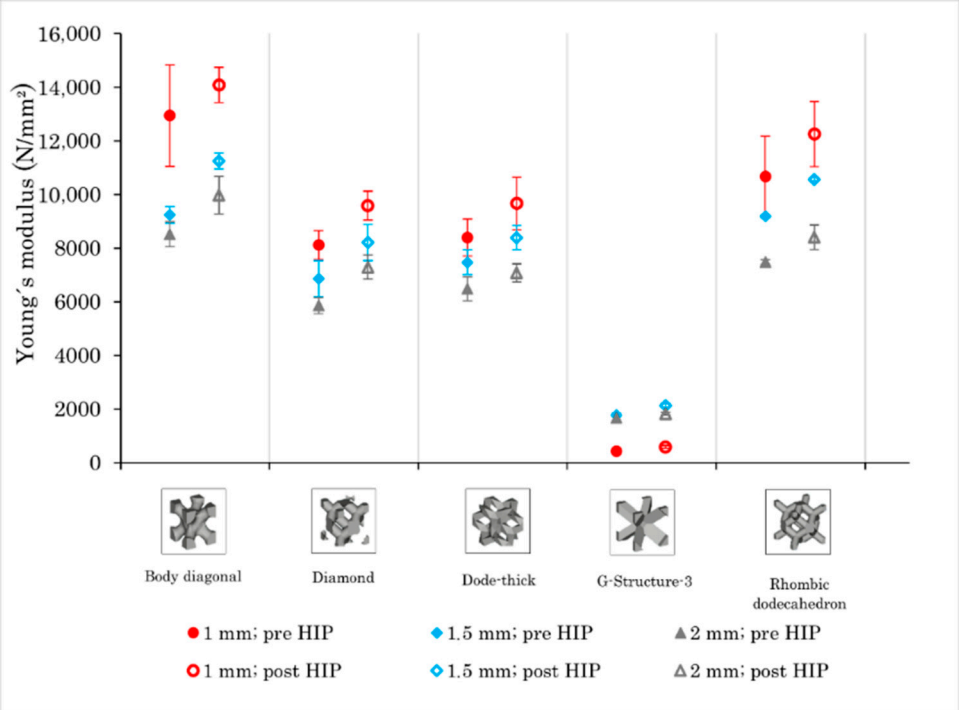

Figure 6. Young's modulus of different lattice structures as a function of lattice size and HIP.

To avoid the fracture of an implant during a high load, the fracture stress should be as high as possible. The fracture stress for different lattice structures and elementary cell sizes is summarized in Figure 7. For all lattice structures, a high fracture strength is accompanied with a high Young's modulus (see Figure 6). In contrast to the Young's modulus, hot isostatic pressing has no definite impact on the fracture stress, showing only a minor influence in both directions of higher or lower fracture stress for the different lattice structures and elementary cell sizes. In contrast to these measurements, in the literature, HIP treatment of Ti–6Al–2Zr–1Mo–1V is reported to result in a 15% increase in tensile strength [32]. However, the influence of the elementary cell size reveals an increasing fracture stress with decreasing cell size, except for the G-structure, a behavior similarly found for the Young's modulus. The cell type with the highest fracture stress is the Body

diagonal, while the G-structure has the lowest stress, which in turn is roughly in accordance with the relative density (see Figure 2).

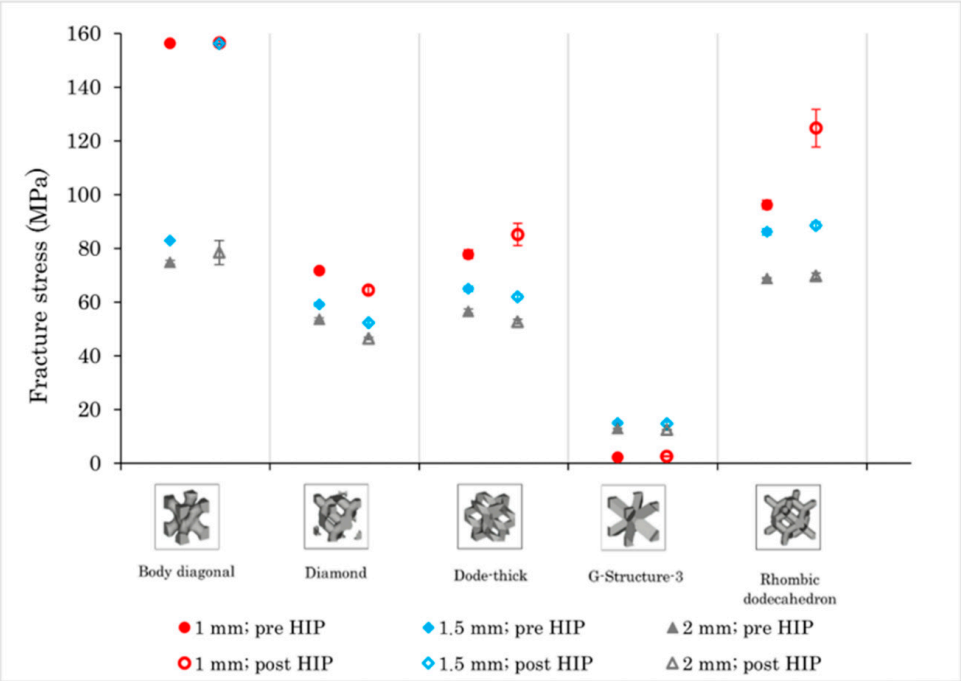

Figure 7. Fracture stress of different lattice structures as a function of lattice size and HIP.

With regard to the desired application and the required mechanical properties, a fracture stress above 11 MPa and a low Young's modulus are necessary. Based on the results discussed above, therefore, certain structures and parameter combinations can be excluded. For instance, the fracture stress of the G-structure depends on the cell size in the same range or below the collapse load of a natural intervertebral disc of 11 MPa [48]. Hence, the G-structure can be omitted. All structures with an elementary cell size of 1 mm can be excluded because of the high Young's modulus and the high deviation. Because of its high Young's modulus, the Body diagonal structure and the rhombic dodecahedron with 1.5 mm elementary cell size are also disqualified. The remaining structures and parameter combinations are characterized by a sufficiently high fracture stress and a high elasticity below 7.500 N/mm^2 in the pre-HIP status and below 8.500 N/mm^2 in the post-HIP status.

3.4. Fatigue Behavior

To determine the fatigue behavior, Wöhler tests were carried out, with loads related to the application as an intervertebral disc implant. Thus, three measuring points were defined: 1.9 kN, which corresponds to the compressive force in the lumbar intervertebral disc when lifting 10 kg; 9 kN, corresponding to the maximum compressive force occurring in the lumbar intervertebral disc during the stooped lifting of more than 50 kg; and 13.5 kN, which includes a safety factor of 1.5 times the maximum load. A specimen was considered suitable if its fatigue resistance in the load range of 1.9 kN withstood the load for more than 10^6 cycles, which corresponds to about 100 lifts per day for 30 years. In case of a failure of a sample, the cycles to failure were recorded.

The results for the pre-HIP samples of the remaining lattice structures, i.e., after the exclusion of certain selected structures discussed in the previous section, are depicted in a Wöhler curve in Figure 8. Only the test specimen with dode-thick lattice and 1.5 mm elementary cell size fulfilled the required fatigue strength under a load of 1.9 kN. All other specimens displayed anterior fracture. Furthermore, it can be stated that the test specimen rhombic dodecahedron with 2 mm elementary cell size exhibited the highest strength at high loads and a low number of cycles before fracture but showed a disproportionately

high decrease of the stress amplitude to failure at a high number of cycles. The diamond-30-percent-relative-density structure with an elementary cell size of 2 mm, on the other hand, exhibited the lowest strength at all numbers of cycles. Diamond-30 and dode-thick structures exhibited comparable densities; any differences might be attributed to the number of the struts of these lattice structures, which determine the Maxwell criterion of cell-based lattice structures, and thus the dominating load response type, and to the geometry of the struts (round bars for Diamond-30 and triangular bars for dode-thick; see Section 2.2). In addition, such geometries may exhibit differences in microstructure quality.

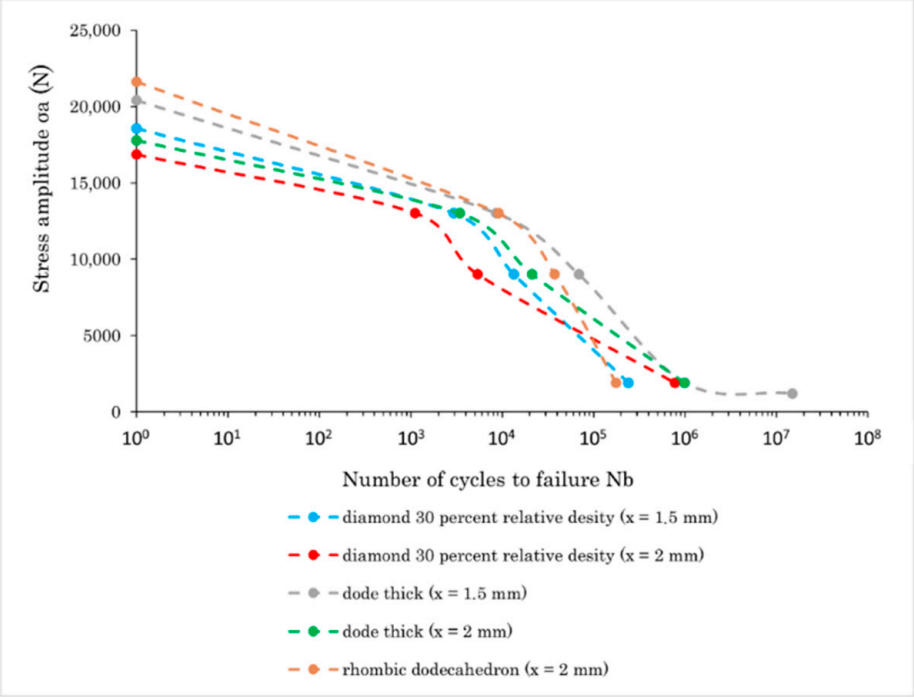

Figure 8. Fatigue behavior of different lattice structures pre-HIP.

Overall, the pre-HIP structures revealed a major lack of fatigue strength at low loads and a high number of cycles. This is attributed to defects like pores and micro cracks during the LPBF process [22,23], which grow and propagate slowly in volume with an increasing number of cycles [24].

In addition, the post-HIP samples were dynamically tested to determine the influence of hot isostatic pressing on the fatigue behavior. The results of the fatigue tests are shown in Figure 9 and reveal no major differences to Figure 8, i.e., to the pre-HIP status, at one cycle and also no clear influence at loads of 13 kN and 9 kN. Looking at the low load part of the curve with 1.9 kN load, it can be seen that all specimens withstand the load for 10^6 cycles and the 1.2 kN load for 10^7 cycles. The dynamic load capacity increases significantly at a low load and a high number of cycles in comparison to the specimen pre-HIP.

The optical examination of the specimen shows a similar behavior to the static compression tests, as shown in Figure 5. While the pre-HIP components tend to show shear fracture as reported in the literature [52], the post-HIP components show an increased tendency to severe deformations and displacements of the lattice planes. This is particularly evident in the fact that some post-HIP components reveal a strong deformation of lattice planes and, in some cases, shear fractures of individual areas, but the component as a whole does not show total failure similar to Figure 5a.

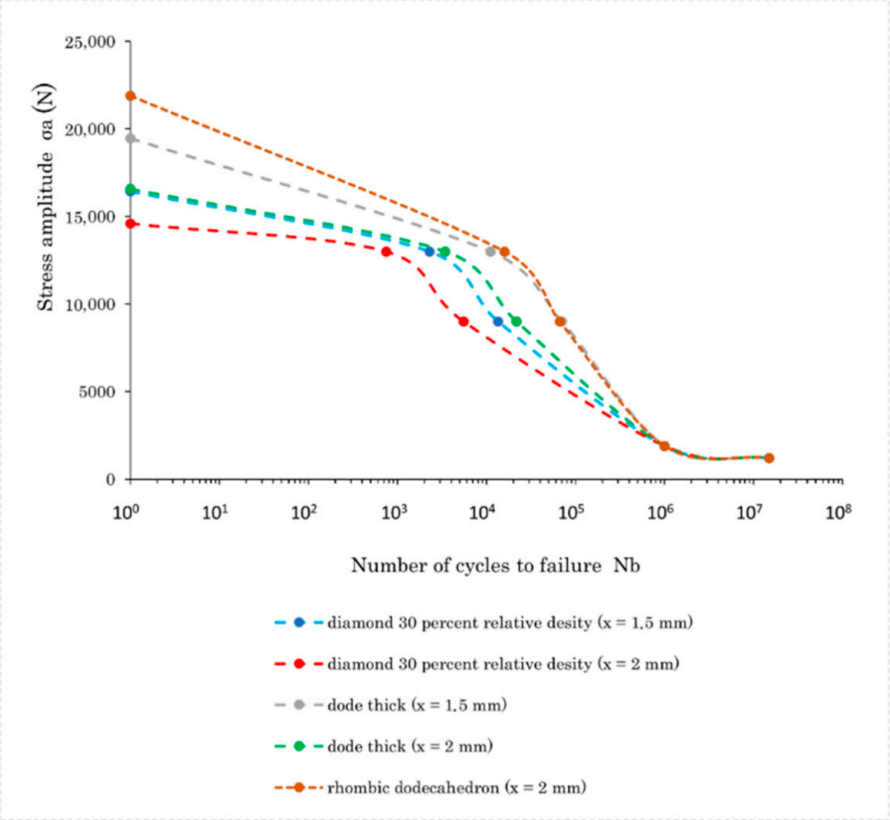

Figure 9. Fatigue behavior of different lattice structures post-HIP.

4. Discussion

In both the static and the dynamic compression tests, a significant influence of hot isostatic pressing on the examined components is found. In the static compression tests, it is particularly noticeable that the plastic range of the stress–strain diagram is significantly larger for post-HIP specimens as compared to the pre-HIP status. This agrees with the literature results, revealing a higher fracture strain after heat treatment [43]. This can be explained by the reduction of residual stresses during hot isostatic pressing, which results in a larger elongation capacity. In addition, an ambiguous influence on the fracture stress is measured, which can be attributed to the reduction of residual stress after HIP, which decreases the fracture stress. Without hot isostatic pressing (pre-HIP status), these stresses counteract the forces acting from outside and thus require a higher force to destroy the component; after hot isostatic pressing (post HIP status) no internal stresses counteract the forces from the outside, e.g., its fracture occurs at a lower stress than pre HIP [53]. Moreover, a reduction of pores and micro cracks during the HIP process increases the fracture stress, which counteracts the loss of internal stresses, and the influence of the HIP process results are ambiguous as measured.

The examination of the dynamic load revealed that only one pre-HIP sample fulfills the requirement of withstanding 10^6 cycles (dode-thick with 1.5 mm cell size). After heat treatment, however, the strength of the samples increases significantly at a low load and high number of cycles. At a high number of cycles, cracking occurs from defects such as pores or micro cracks [25,46]. Pre-HIP components have a large number of defects inside or on the surface of the component, while the inner defects are reduced in size and number by hot isostatic pressing [31]. So, the crack growth, as occurring pre HIP, can consequently be prevented or significantly delayed. In the case of high stress and low cycle numbers, on the other hand, the behavior is different. However, hot isostatic pressing, at least with the prescribed process parameters, leads to a coarsening of the microstructure test specimen

post HIP and can have a similar or lower load capacity compared to a test specimen pre HIP at high stress and low number of cycles.

For the selection of a suitable unit cell and thus for the optimization of the mechanical properties of an intervertebral disc implant, it is essential to consider the results of the static and dynamic tests. The static compression tests can be used to determine these specimens, which exhibit a sufficiently high fracture stress, and simultaneously the Young's modulus is kept comparatively low. The dynamic investigations post HIP initially suggest that all components exhibit a sufficiently high fatigue strength. However, the optical examination reveals that although there is no total failure of the specimens, most of the specimens show deformations and/or partial fractures. Only the rhombic dodecahedron with 2 mm cell size and dode-thick specimen with 1.5 mm cell size do not show any detectable defects after 10^6 cycles.

Detailed examination of the static compression tests of the most promising lattice types in Figure 6 reveals that the dode-thick specimen with an elementary cell size of 1.5 mm has the same Young's modulus as the rhombic specimen. In addition, the dynamic compression tests show that this elementary cell offers sufficiently high strength of more than 70,000 cycles, even at the typically occurring maximum force of 9 kN. Furthermore, sufficient fatigue strength at 1.9 kN is already present before hot isostatic pressing. The dode-thick elementary cell proves to be particularly promising in comparison with the rhombic dodecahedron cell, especially for the everyday load cases of 1.9 kN or 9 kN (Table 1).

Table 1. Static and dynamic properties of the most suitable lattice structures.

Geometry	Status	Young's Modulus (N/mm^2)	Fracture Stress (MPa)	Cycles at Fracture		
				1300 N	9000 N	1900 N
Rhombic dodecahedron (x = 2 mm)	Pre-HIP	7477	68	9169	37,602	176,156
	Post-HIP	8406	69	15,963	66,452	$>10^6$
Dode-thick (x = 1.5 mm)	Pre-HIP	7476	64	8605	68,790	$>10^6$
	Post-HIP	8395	61	11,021	70,072	$>10^6$

In summary, it can be stated that the mechanical optimization of the component in order to achieve the lowest possible Young's modulus combined with a high fatigue strength can be realized by selecting a suitable lattice structure. In comparison to massive titanium with a Young's modulus of 110 kN/mm^2, the Young's modulus is reduced by using lattice structures of about 93%. Taking into account the results obtained, the dode-thick specimen with an elementary cell size of 1.5 mm proves to be the most promising for this purpose.

5. Conclusions

We compared the mechanical load properties of five Ti-6Al-4V lattice structure types with different elementary cell sizes built by laser powder bed fusion. In addition, the impact of hot isostatic pressing on the load capabilities under static and dynamic compression was studied. For comparison, the Young's modulus, the fracture stress and the cycles to failure were measured in order to evaluate the potential use of the lattice structures as medical intervertebral disc implants. In the static compression tests, the post HIP samples reveal a much higher strain, higher Young's modulus and a similar fracture stress. While samples without hot isostatic pressing reveal a shear fracture, the hot isostatic pressed samples have a high ductile area, where the lattice layers are wrapped and pressed into the underlying layers without fracture. In the dynamic tests, in the high load area no significant influence of the HIP process is measured, while in the high cycle low load regime the pre-HIP samples break, but the post samples survive the test. Overall, dode-thick and rhombic dodecahedron structures with 2 mm and 1.5 mm elementary cell size reveal no damage after 10^6 cycles and are recommended for the application due to their low Young's modulus.

Author Contributions: Conceptualization, B.A. and R.H.; methodology, B.A. and R.H.; software, B.A; validation, B.A.; formal analysis, B.A.; investigation, B.A.; resources, R.H.; data curation, B.A.; writing—original draft preparation, B.A. and R.H.; writing—review and editing, B.A. and R.H.; visualization, B.A.; supervision, R.H.; project administration, R.H. All authors have read and agreed to the published version of the manuscript.

Funding: This research received no funding.

Data Availability Statement: Not applicable.

Acknowledgments: We thank Melanie Abb for fruitful support and participating in conducting the experimental work.

Conflicts of Interest: The authors declare no conflict of interest.

References

1. Ferrucci, L.; Cooper, R.; Shardell, M.; Simonsick, E.M.; Schrack, J.A.; Kuh, D. Age-Related Change in Mobility: Perspectives From Life Course Epidemiology and Geroscience. *J. Gerontol. Ser. A Biol. Sci. Med. Sci.* **2016**, *71*, 1184–1194. [CrossRef] [PubMed]
2. Keehan, S.P.; Stone, D.A.; Poisal, J.A.; Cuckler, G.A.; Sisko, A.M.; Smith, S.D.; Madison, A.J.; Wolfe, C.J.; Lizonitz, J.M. National Health Expenditure Projections, 2016–2025: Price Increases, Aging Push Sector To 20 Percent Of Economy. *Health Aff. (Proj. Hope)* **2017**, *36*, 553–563. [CrossRef]
3. McInnes, L. Importance of maintaining mobility to elderly health. *Aging Health* **2011**, *7*, 165–167. [CrossRef]
4. *ISO/ASTM 52900:2015, ISO/TC 261*; Additive Manufacturing—General Principles—Terminology. International Organization for Standardization: Geneva, Switzerland, 2015.
5. Li, Y.; Ding, Y.; Munir, K.; Lin, J.; Brandt, M.; Atrens, A.; Xiao, Y.; Kanwar, J.R.; Wen, C. Novel β-Ti35Zr28Nb alloy scaffolds manufactured using selective laser melting for bone implant applications. *Acta Biomater.* **2019**, *87*, 273–284. [CrossRef] [PubMed]
6. Niinomi, M.; Nakai, M. Titanium-Based Biomaterials for Preventing Stress Shielding between Implant Devices and Bone. *Int. J. Biomater.* **2011**, *2011*, 836587. [CrossRef]
7. Wu, Z.; Dai, Y.; Luo, J.; Ji, X.; Xie, Z.; Li, L.; Xie, X. Physiochemical and biological evaluation of SLM-manufactured Ti-10Ta-2Nb-2Zr alloy for biomedical implant applications. *Biomed. Mater.* **2020**, *15*, 45017. [CrossRef]
8. Iwaya, Y.; Machigashira, M.; Kanbara, K.; Miyamoto, M.; Noguchi, K.; Izumi, Y.; Ban, S. Surface properties and biocompatibility of acid-etched titanium. *Dent. Mater. J.* **2008**, *27*, 415–421. [CrossRef]
9. Eisenbarth, E.; Velten, D.; Müller, M.; Thull, R.; Breme, J. Biocompatibility of beta-stabilizing elements of titanium alloys. *Biomaterials* **2004**, *25*, 5705–5713. [CrossRef]
10. Adelmann, B.; Abb, M.; Hellmann, R. Comparative study of cell growth and cellular adhesion on Ti-6Al-4V surfaces made by Selective Laser Melting followed by different surface post processing steps. *IOP Conf. Ser. Mater. Sci. Eng.* **2021**, *1135*, 12028. [CrossRef]
11. Sidambe, A.T. Biocompatibility of Advanced Manufactured Titanium Implants-A Review. *Materials* **2014**, *7*, 8168–8188. [CrossRef]
12. Matena, J.; Petersen, S.; Gieseke, M.; Kampmann, A.; Teske, M.; Beyerbach, M.; Escobar, H.M.; Haferkamp, H.; Gellrich, N.-C.; Nolte, I. SLM produced porous titanium implant improvements for enhanced vascularization and osteoblast seeding. *Int. J. Mol. Sci.* **2015**, *16*, 7478–7492. [CrossRef] [PubMed]
13. Edelmann, A.; Dubis, M.; Hellmann, R. Selective Laser Melting of Patient Individualized Osteosynthesis Plates-Digital to Physical Process Chain. *Materials* **2020**, *13*, 5786. [CrossRef]
14. Fousová, M.; Kubásek, J.; Vojtěch, D.; Fojt, J.; Čapek, J. 3D printed porous stainless steel for potential use in medicine. *IOP Conf. Ser. Mater. Sci. Eng.* **2017**, *179*, 12025. [CrossRef]
15. Arabnejad, S.; Johnston, B.; Tanzer, M.; Pasini, D. Fully porous 3D printed titanium femoral stem to reduce stress-shielding following total hip arthroplasty. *J. Orthop. Res. Off. Publ. Orthop. Res. Soc.* **2017**, *35*, 1774–1783. [CrossRef] [PubMed]
16. Leordean, D.; Dudescu, C.; Marcu, T.; Berce, P.; Balc, N. Customized implants with specific properties, made by selective laser melting. *Rapid Prototyp. J.* **2015**, *21*, 98–104. [CrossRef]
17. Yılmaz, E.; Gökçe, A.; Findik, F.; Gulsoy, H.O.; İyibilgin, O. Mechanical properties and electrochemical behavior of porous Ti-Nb biomaterials. *J. Mech. Behav. Biomed. Mater.* **2018**, *87*, 59–67. [CrossRef]
18. Hao, L.; Dadbakhsh, S.; Seaman, O.; Felstead, M. Selective laser melting of a stainless steel and hydroxyapatite composite for load-bearing implant development. *J. Mater. Process. Technol.* **2009**, *209*, 5793–5801. [CrossRef]
19. Chan, K.S.; Koike, M.; Mason, R.L.; Okabe, T. Fatigue Life of Titanium Alloys Fabricated by Additive Layer Manufacturing Techniques for Dental Implants. *Metall. Mater. Trans. A* **2013**, *44*, 1010–1022. [CrossRef]
20. Okazaki, Y.; Ito, Y.; Kyo, K.; Tateishi, T. Corrosion resistance and corrosion fatigue strength of new titanium alloys for medical implants without V and Al. *Mater. Sci. Eng. A* **1996**, *213*, 138–147. [CrossRef]
21. Shemtov-Yona, K.; Rittel, D. Fatigue of Dental Implants: Facts and Fallacies. *Dent. J.* **2016**, *4*, 16. [CrossRef]
22. Glodez, S.; Klemenc, J.; Zupanic, F.; Vesenjak, M. High-cycle fatigue and fracture behaviours of SLM AlSi10Mg alloy. *Trans. Nonferrous Met. Soc. China* **2020**, *30*, 2577–2589. [CrossRef]

23. Koutiri, I.; Pessard, E.; Peyre, P.; Amlou, O.; de Terris, T. Influence of SLM process parameters on the surface finish, porosity rate and fatigue behavior of as-built Inconel 625 parts. *J. Mater. Process. Technol.* **2018**, *255*, 536–546. [CrossRef]
24. Kan, W.H.; Chiu, L.N.S.; Lim, C.V.S.; Zhu, Y.; Tian, Y.; Jiang, D.; Huang, A. A critical review on the effects of process-induced porosity on the mechanical properties of alloys fabricated by laser powder bed fusion. *J. Mater. Sci.* **2022**, *57*, 9818–9865. [CrossRef]
25. Leuders, S.; Vollmer, M.; Brenne, F.; Tröster, T.; Niendorf, T. Fatigue Strength Prediction for Titanium Alloy TiAl6V4 Manufactured by Selective Laser Melting. *Metall. Mater. Trans. A* **2015**, *46*, 3816–3823. [CrossRef]
26. Ferreira, F.F.; Neto, D.M.; Jesus, J.S.; Prates, P.A.; Antunes, F.V. Numerical Prediction of the Fatigue Crack Growth Rate in SLM Ti-6Al-4V Based on Crack Tip Plastic Strain. *Metals* **2020**, *10*, 1133. [CrossRef]
27. Ngnekou, J.N.D.; Nadot, Y.; Henaff, G.; Nicolai, J.; Ridosz, L. Influence of defect size on the fatigue resistance of AlSi10Mg alloy elaborated by selective laser melting (SLM). *Procedia Struct. Integr.* **2017**, *7*, 75–83. [CrossRef]
28. Biffi, C.A.; Fiocchi, J.; Bassani, P.; Paolino, D.S.; Tridello, A.; Chiandussi, G.; Rossetto, M.; Tuissi, A. Microstructure and preliminary fatigue analysis on AlSi10Mg samples manufactured by SLM. *Procedia Struct. Integr.* **2017**, *7*, 50–57. [CrossRef]
29. Yadav, P.; Rigo, O.; Arvieu, C.; Le Guen, E.; Lacoste, E. In Situ Monitoring Systems of The SLM Process: On the Need to Develop Machine Learning Models for Data Processing. *Crystals* **2020**, *10*, 524. [CrossRef]
30. Tillmann, W.; Schaak, C.; Nellesen, J.; Schaper, M.; Aydinöz, M.E.; Hoyer, K.-P. Hot isostatic pressing of IN718 components manufactured by selective laser melting. *Addit. Manuf.* **2017**, *13*, 93–102. [CrossRef]
31. Jamshidi, P.; Aristizabal, M.; Kong, W.; Villapun, V.; Cox, S.C.; Grover, L.M.; Attallah, M.M. Selective Laser Melting of Ti-6Al-4V: The Impact of Post-processing on the Tensile, Fatigue and Biological Properties for Medical Implant Applications. *Materials* **2020**, *13*, 2813. [CrossRef]
32. Cai, C.; Gao, X.; Teng, Q.; Kiran, R.; Liu, J.; Wei, Q.; Shi, Y. Hot isostatic pressing of a near α-Ti alloy: Temperature optimization, microstructural evolution and mechanical performance evaluation. *Mater. Sci. Eng. A* **2021**, *802*, 140426. [CrossRef]
33. Aboulkhair, N.T.; Maskery, I.; Tuck, C.; Ashcroft, I.; Everitt, N.M. The microstructure and mechanical properties of selectively laser melted AlSi10Mg: The effect of a conventional T6-like heat treatment. *Mater. Sci. Eng. A* **2016**, *667*, 139–146. [CrossRef]
34. Sistiaga, M.L.M.; Hautfenne, S.N.C.; van Humbeeck, J. Effect of Heat Treatment Of 316L Stainless Steel Produced by Selective Laser Melting (SLM). In Proceedings of the 27th Annual International Solid Freeform Fabrication Symposium—An Additive Manufacturing Conference, Austin, TX, USA, 8–10 August 2016; University of Texas: Austin, TX, USA, 2016; pp. 558–565.
35. Spierings, A.B.; Dawson, K.; Kern, K.; Palm, F.; Wegener, K. SLM-processed Sc- and Zr- modified Al-Mg alloy: Mechanical properties and microstructural effects of heat treatment. *Mater. Sci. Eng. A* **2017**, *701*, 264–273. [CrossRef]
36. van Hooreweder, B.; Kruth, J.-P. Advanced fatigue analysis of metal lattice structures produced by Selective Laser Melting. *CIRP Ann.* **2017**, *66*, 221–224. [CrossRef]
37. Greitemeier, D.; Palm, F.; Syassen, F.; Melz, T. Fatigue performance of additive manufactured TiAl6V4 using electron and laser beam melting. *Int. J. Fatigue* **2017**, *94*, 211–217. [CrossRef]
38. Rans, C.; Michielssen, J.; Walker, M.; Wang, W.; Hoen-Velterop, L. Beyond the orthogonal: On the influence of build orientation on fatigue crack growth in SLM Ti-6Al-4V. *Int. J. Fatigue* **2018**, *116*, 344–354. [CrossRef]
39. Sangid, M.D.; Book, T.A.; Naragani, D.; Rotella, J.; Ravi, P.; Finch, A.; Kenesei, P.; Park, J.-S.; Sharma, H.; Almer, J.; et al. Role of heat treatment and build orientation in the microstructure sensitive deformation characteristics of IN718 produced via SLM additive manufacturing. *Addit. Manuf.* **2018**, *22*, 479–496. [CrossRef]
40. Cai, C.; Qiu, J.C.D.; Shian, T.W.; Han, C.; Liu, T.; Kong, L.B.; Srikanth, N.; Sun, C.-N.; Zhou, K. Laser powder bed fusion of Mo2C/Ti-6Al-4V composites with alternately laminated α'/β phases for enhanced mechanical properties. *Addit. Manuf.* **2021**, *46*, 102134. [CrossRef]
41. Yılmaz, E.; Gökçe, A.; Findik, F.; Gulsoy, H.Ö. Assessment of Ti–16Nb–xZr alloys produced via PIM for implant applications. *J. Therm. Anal. Calorim.* **2018**, *134*, 7–14. [CrossRef]
42. Yılmaz, E.; Gökçe, A.; Findik, F.; Gulsoy, H. Metallurgical properties and biomimetic HA deposition performance of Ti-Nb PIM alloys. *J. Alloys Compd.* **2018**, *746*, 301–313. [CrossRef]
43. Vrancken, B.; Thijs, L.; Kruth, J.-P.; van Humbeeck, J. Heat treatment of Ti6Al4V produced by Selective Laser Melting: Microstructure and mechanical properties. *J. Alloys Compd.* **2012**, *541*, 177–185. [CrossRef]
44. Agius, D.; Kourousis, K.; Wallbrink, C. A Review of the As-Built SLM Ti-6Al-4V Mechanical Properties towards Achieving Fatigue Resistant Designs. *Metals* **2018**, *8*, 75. [CrossRef]
45. Speirs, M.; van Hooreweder, B.; van Humbeeck, J.; Kruth, J.-P. Fatigue behaviour of NiTi shape memory alloy scaffolds produced by SLM, a unit cell design comparison. *J. Mech. Behav. Biomed. Mater.* **2017**, *70*, 53–59. [CrossRef] [PubMed]
46. Refai, K.; Brugger, C.; Montemurro, M.; Saintier, N. An experimental and numerical study of the high cycle multiaxial fatigue strength of titanium lattice structures produced by Selective Laser Melting (SLM). *Int. J. Fatigue* **2020**, *138*, 105623. [CrossRef]
47. Fritsch, E.W.; Pitzen, T. Zervikale Bandscheibenprothesen. *Der. Orthop.* **2006**, *35*, 347–359. [CrossRef]
48. Wintermantel, E.; Ha, S.-W. (Eds.) *Medizintechnik: Life Science Engineering*, 5th ed.; Springer: Berlin/Heidelberg, Germany, 2009.
49. Ahmadi, M.; Karpat, Y.; Acar, O.; Kalay, Y.E. Microstructure effects on process outputs in micro scale milling of heat treated Ti6Al4V titanium alloys. *J. Mater. Process. Technol.* **2018**, *252*, 333–347. [CrossRef]
50. Maskery, I.; Aremu, A.O.; Simonelli, M.; Tuck, C.; Wildman, R.D.; Ashcroft, I.A.; Hague, R. Mechanical Properties of Ti-6Al-4V Selectively Laser Melted Parts with Body-Centred-Cubic Lattices of Varying cell size. *Exp. Mech.* **2015**, *55*, 1261–1272. [CrossRef]

51. Sun, S.; Teng, Q.; Xie, Y.; Liu, T.; Ma, R.; Bai, J.; Cai, C.; Wei, Q. Two-step heat treatment for laser powder bed fusion of a nickel-based superalloy with simultaneously enhanced tensile strength and ductility. *Addit. Manuf.* **2021**, *46*, 102168. [CrossRef]
52. Mazur, M.; Leary, M.; Sun, S.; Vcelka, M.; Shidid, D.; Brandt, M. Deformation and failure behaviour of Ti-6Al-4V lattice structures manufactured by selective laser melting (SLM). *Int. J. Adv. Manuf. Technol.* **2015**, *84*, 1391–1411. [CrossRef]
53. Kumar, P.; Ramamurty, U. Microstructural optimization through heat treatment for enhancing the fracture toughness and fatigue crack growth resistance of selective laser melted Ti 6Al 4V alloy. *Acta Mater.* **2019**, *169*, 45–59. [CrossRef]